Carbon Trends 19 (2025) 100466

Contents lists available at ScienceDirect

Carbon Trends

journal homepage: www.elsevier.com/locate/cartre

Developing a density functional theory model of glassy carbon via carbon defect induction and relaxation

K. Meerholz [a], A. Falch [b,c], C.G.C.E. van Sittert [a,*]

[a] Laboratory for Applied Molecular Modelling, Research Focus Area: Chemical Resource Beneficiation, North-West University, 11 Hoffman Street, 2520, South Africa
[b] Electrochemistry for Energy & Environment Group, Research Focus Area: Chemical Resource Beneficiation (CRB), North-West University, Private Bag X6001, Potchefstroom 2520, South Africa
[c] School of Chemistry, Molecular Sciences Institute, University of the Witwatersrand, Johannesburg, 2000, South Africa

ARTICLE INFO

Keywords:
Glassy carbon
Density functional theory
Structural modelling
X-ray diffraction
Electrode substrate

ABSTRACT

Glassy Carbon (GC) is a non-graphitising carbon known for its thermal stability, conductivity, and resistance to chemical attack, making it valuable in industrial and scientific applications, especially as an electrode substrate in catalysis research. Despite its widespread use, GC's precise structural characteristics is unclear due to synthesis variability. This study developed and validated a computational model to simulate GC's structure. Starting from the R3-carbon allotrope, density functional theory calculations were used to construct a representative GC model, incorporating induced defects to mimic its structural imperfections. Multiple GC slab models were created for comparative analysis. Validation involved comparing theoretical X-ray diffraction data with published data, confirming the model's accuracy in representing the GC's structure. The model showed high correlation with existing models, particularly those by Jurkiewicz et al., emphasizing the effect of formation temperature on GC's structural evolution. These findings enhance the understanding of GC's structural complexities, providing a solid foundation for future research and applications in material science, especially for robust and conductive substrates used in electrocatalysis.

1. Introduction

Glassy carbon (GC) is classified as a non-graphitising form of carbon [1], which is a form of carbon that contains low amounts of hydrogen or oxygen and retains its structure at high temperatures (up to 3000 °C). Due to its unique physical and chemical properties, GC, also known as vitreous carbon, is widely used as a substrate material in industrial and laboratory applications. These properties include high conductivity, low resistance, non-reactivity towards acids and bases, hardness, and closed porosity [1–3]. Because of these attributes, GC is particularly well-suited as an electrode substrate for catalyst research, since various metal catalysts are subjected to harsh chemical environments, making the robustness of the substrate crucial [4]. GC's innate resistance to chemical reactions and its closed porosity prevent unwanted reactions or corrosion of the substrate, ensuring the integrity of experimental data when using GC as a substrate or electrochemical electrode. Simultaneously, its excellent electrical conductivity facilitates precise and efficient electrochemical measurements.

Although GC, as material has been used in various scientific and industrial applications since the early 1960s [5], its structural characteristics remains uncertain. This uncertainty is further compounded by the considerable variability observed in the structure of glassy carbon, a phenomenon primarily dictated by factors such as the synthesis temperature and the purity of the carbon source utilised. Consequently, the need for a universally applicable model that can effectively describe the structural configurations inherent to GC remains. Hence, a thorough exploration of the factors shaping glassy carbon's formation is crucial to understand its complexities.

In a comprehensive review by Harris et al. [6], various models describing the structural attributes of GC have been discussed. Among these, Crawford et al. [7] initially proposed that GC, is composed of tightly packed layers resembling folded graphite sheets. An alternative hypothesis by Jenkins et al. [8] posited that GC structure is a complex matrix of interwoven carbon fibre ribbons, the observed low density is attributed to the interstitial spaces between these ribbons. While these models have significantly contributed to the understanding of GC structural composition, it is imperative to note their respective limitations. For instance, the model proposed by Crawford et al. [7] fails to

* Corresponding author.
E-mail address: Cornie.VanSittert@nwu.ac.za (C.G.C.E. van Sittert).

https://doi.org/10.1016/j.cartre.2025.100466
Received 29 August 2024; Received in revised form 9 January 2025; Accepted 9 January 2025
Available online 10 January 2025

account for the absence of detectable pores within the structure, a feature implicitly suggested by their model. In contrast, Jenkins et al. [8] model successfully addresses this lack of porosity but lacks an explanation for the intricate formation of folded graphite sheets.

However, later in 2004 Harris et al. [2] suggested that GC exhibits structural characteristics similar to fullerenes. This model provided a more robust framework for understanding the closed porosity exhibited by GC. Further validation of Harris's model was achieved through molecular models constructed by classical analytical techniques such as X-ray diffraction (XRD) and high-resolution transmission electron microscopy [9–11].

In order to further clarify the structures of GC, various studies have been carried out using high-resolution transmission electron microscopy [6], Raman spectroscopy [12,13], X-ray photoelectron spectroscopy [13], X-ray small-angle scattering [14], wide-angle X-ray scattering [10], neutron [15] and X-ray diffraction [13]. Many of these studies have shown evidence of non-hexagonal rings in curved carbon sheets. They proposed a fullerene-related structure for GC, where pentagons and heptagons are dispersed among hexagons, forming a network with single-point structural defects [16,17] known as Stone-Wales defects, which transform hexagons into pentagons or heptagons [18]. This fullerene-related configuration is further supported by the presence of polyhedral graphite crystals in GC, as identified by Gogotsi et al. [19], and studies by Hawelek et al. [9], reinforcing the plausibility of this structural model.

In 2017 Jurkiewicz et al. [11] created models of GC synthesised at various temperatures between 800 °C and 2500 °C. These GC models were constructed using molecular dynamics, based on data obtained from high-resolution transmission electron microscopy, neutron and XRD results. Notably, this groundbreaking model was grounded in an extensive body of research spanning activated carbon and other carbon allotropes [17,20–24]. Furthermore, it highlighted the influence of pyrolysis temperature on the structural evolution of GC. As the temperature was elevated, an evident transformation towards a more "graphite-like" configuration with increasingly uniform carbon-carbon distribution within the layers became evident.

The current study aims to establish a comprehensive and representative computational model of GC, based on density functional theory (DFT) calculations, for utilisation as a foundational substrate in subsequent investigations. The model's construction will begin with a variation of carbon [25], namely the R3-carbon allotrope with the space group R3¯m, which exhibit significant similarities to the properties of GC. Using solid-state DFT, a carbon-layered periodic system resembling the characteristics of GC will be created. This model will be constructed by introducing single point defects into the pristine slab and preforming a geometric optimisation and will henceforth be referred to as Defect Induced Glassy Carbon (DI-GC) model. This approach will simulate the features found in the GC structure by allowing it to attain a relaxed state after addition of the defects.

To validate the DI-GC model, theoretical XRD spectra will be generated and compared against theoretical XRD spectra generated for the GC models developed by Jurkiewicz et al. [11]. Their models were developed by using neutron diffraction and XRD data to obtaining atom positions and molecular dynamics to optimise the structure.

The comparative analysis serves to verify that the structural attributes of GC emerge because of the lattice imperfections intentionally introduced during the model's optimisation process This comprehensive approach not only seeks to create a robust GC model but also to establish a foundation for future research involving this unique carbon material. The increasing demand for molecular models encompassing various facets of material research has prompted the necessity for the development of a comprehensive solid-state GC model, which holds the potential to catalyse further advancements in specialised domains like electrocatalyst research, where GC serves as a pivotal substrate for catalytic investigations.

2. Methodology

2.1. General

This study was conducted by employing the Cambridge Serial Total Energy Package (CASTEP) as an essential computational tool, which operates within the Materials Studio 2020 software package provided by Dassault Systèmes BIOVIA [26]. CASTEP, being a widely recognised solid-state modelling application, is rooted in the principles of DFT [27]. The calculations were performed on high performance computing resources of the Lengau cluster, which is housed at the Centre for High Performance Computing [28] in South Africa. The Lengau cluster utilises 1368 compute nodes with 24 CPU cores and 64 GB RAM per node with a total of 4 PB of storage. Most calculations were conducted using 4 nodes per calculation.

2.2. Unit cell and bulk structure

The triagonal unit cell of the R3 allotrope of carbon was based on work done by Trucano et al. [29] and crystallographic data published by Nixon et al. [30] and obtained from the Materials Project database [31]. The unit cell consists of a trigonal crystal system (α & β = 90°and γ = 120°) with a rhombohedral lattice (a & b = 2.46 Å and c = 33.19 Å) with group number 166 and space group R3¯m. A table containing the fraction coordinates of the R3 unit cell can be found in the Supplementary Information (Table S1).

The unit cell was expanded to a 2 × 2 × 2 bulk structure. The unit cell and bulk structure were geometrically optimised using the generalised gradient approximation functional developed by Perdew, Burke and Ernzerhof [32] (GGA-PBE). A Monkhorst Pack k-point grid [33] of 5 × 5 × 5 was used in the integration of the reciprocal space. The kinetic energy cut-off was set at 400 eV with the Ultrasoft pseudopotentials. The plane-wave basis was obtained using Koelling-Hamon relativistic treatment approach [34]. The convergence algorithm used was the Two-Point Steepest Descent (TPSD) and the cell optimisation was achieved using a SCF tolerance of 1.0 × 10^{-6} eV/atom. The convergence energy was set to 2.0e^{-5} eV/atom, a max force, stress and displacement of 0.05 eV/Å, 0.1 GPa, 0.002 Å was used, respectively. A van der Waals dispersion correction was applied using the many-body dispersion. The number of k-points and the number of layers was analysed to determine the optimum parameters, the k-points were varied from 1 × 1 × 1 to 6 × 6 × 6 and number of layers of carbon were varied from 3 to 12 layers.

2.3. Pristine slabs

In order to create the surface models of the GC, the bulk structure was cut along the 001 Miller plane [25] and a 20 Å vacuum gap was added in the c-direction. The 001 Miller plane was selected for the slab system construction to ensure the model aligns with literature [11,35], because according to XRD results the GC's primitive cell crystal lattice consists of carbon sheets oriented in the (001) direction. A 20 Å vacuum gap was selected since it is large enough to ensure no surface-to-surface interaction. The slab thickness was optimised to ensure there are enough atoms in the lattice to illustrate the effects of the single point defects on the lattice, whilst keeping the model small enough to ensure short computing time. These slabs were geometrically optimised using similar parameters to the bulk structure optimisation. However, the k-points were optimised by varying between 1 × 1 × 1 and 7 × 7 × 1.

2.4. Defect-induced slabs

In this study, the geometrically optimised pristine slabs served as the foundational structure for creating defect-induced slabs. Point defects were introduced into the carbon lattice by systematically eliminating 10 % of the carbon atoms in a stochastic manner. The 10 % threshold was selected based on the empirical findings by Harris et al. [2] and

Jurkiewicz et al. [11], which suggest that GC inherently contains single point defects, constituting, on average, approximately 10 % of the lattice. Consequently, 108 carbon atoms were randomly removed from the lattice, followed by a perturbation of the structure to attain the true ground-state energy configuration. This was achieved by forcing the layers of carbon a few angstroms in the c-axis away from one another that the geometric position of these atoms can again be geometrically relaxed. The system was subsequently relaxed through geometric optimisation, adhering to the same computational settings as for the pristine slabs specifically, employing the GGA-PBE functional with an energy cutoff of 400 eV and a k-point mesh of 7 × 7 × 1. The methodology was repeated to produce multiple slabs with varying defect configurations for further analysis. XRD patterns were obtained for all the slabs utilising the Reflex Tools software Tools in the Materials Studio software [36,37].

2.5. Jurkiewicz models

Jurkiewicz et al. [11] created multiple models of GC (referred to as JGC) at a variety of temperatures, namely 800 °C, 1500 °C, 2000 °C and 2500 °C. (These models will be referred to in the rest of this study as JGC_800, JGC_1500, JGC_2000 and JGC_2500, respectively). These classical molecular models were constructed from graphene layers randomly distributed to simulate a defective graphitic lattice. The graphene layers were randomly translated perpendicular to their stacking direction, simulating a turbostratic arrangement, with the incorporation of structural defects, including Stone-Wales transformations and vacancies, to distort the graphitic structure. These models have different sizes with different atom counts, ranging from 2800 atoms for the 800 °C model, to 24,214 atoms for the 2500 °C model, and thus needed to be standardised. The standardisation was done by cutting representative sections, with the dimensions of a, b = 11.0876 Å and c = 30.0 Å These standardised sections at various formation temperature GC models were, segmented further into nine distinct sections to lower the computational demand, and enhance the representativeness of the XRD spectra.

Fig. 1 illustrates this segmentation process, demonstrating how each standardised GC model was divided (cut) into nine sections from its original in the (001) Miller plane, more extensive structure. The periodic cell dimensions of the nine sections were a, b = 11.0876 Å and c = 30.0 Å Each of the "cuts" were labelled as cut 1 to 9, for example the cut 1 of the 800 °C model will be named JGC_800_cut1. This step was necessary because the original, large theoretical structure could lose detail in the XRD analysis.

Using these cuts the simulated XRD spectra was obtained using the Reflex Tools in the Materials Studio software [36,37].

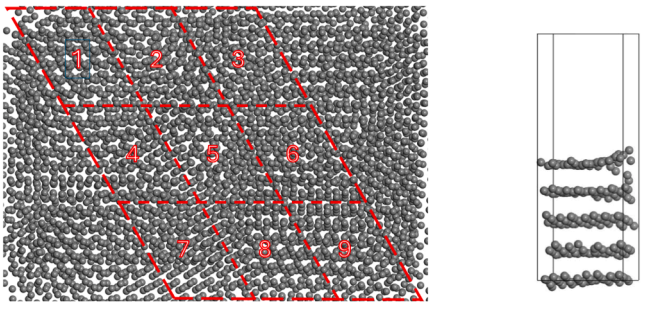

Fig. 1. Classic molecular models developed by Jurkiewicz et al. [11] based on a defective graphitic lattice, which was constructed from graphene layers randomly distributed to introduce disorder. (a) JGC_2000 standardised structure, with the 3 × 3 grid (in red) illustrating how the slab was cut into 9 sections along (001) Miller plane, and (b) an example of the side view of JGC_2000_cut1.

2.6. Reflex tools

In order to obtain theoretical XRD spectra, the tool named Reflex tools [38] which forms part of the Material Studio software was used. This was done on all models including the standardised models based on the models developed by Jurkiewicz et al. [11], to obtain the XRD profiles which were used to compare the systems. The following parameters were configured in the Reflex tools, to simulate XRD patterns. The scan was programmed with a step size of 0.05°, covering a 2θ angle range of 5° to 100°. This specific angular range corresponded to d-spacing values (d_{hkl}) that could be converted to reciprocal lattice vectors with magnitudes ranging from 0.05663 $Å^{-1}$ to 0.9945 $Å^{-1}$. The radiation source selected for the simulation was copper (Cu), emitting X-rays with characteristic wavelengths λ_1 = 1.540562 Å and λ_2 = 1.54439 Å. Note that these wave lengths are predefined by the theoretical radiation source. These wavelengths are widely recognised for their applicability in various XRD studies [39] and offer an excellent resolution for the structures under investigation. The geometry of the XRD lines was configured based on the Bragg-Brentano focusing method [40], a widely adopted approach in X-ray diffractometry. This method is favoured for its ability to deliver high-resolution spectra and is particularly advantageous for samples with layered or textured structures [41,42]. This procedure was iteratively performed, and the resultant XRD spectra were compared against published data [11].

2.7. Radial distribution function

The radial distribution function (RDF) represents the normalized probability density of finding a particle at a distance (r) from a reference particle [43]. It provides insights into how particle density varies with distance and is commonly used to analyse local order and intermolecular interactions in a system. The RDF, denoted as g(r), is calculated using Eq. (1), where the pair distribution function (PDF) at (r) is divided by the average particle density (ρ). The pair distribution function, P(r), as shown in Eq. (2), represents the absolute density of particle pairs within a spherical shell of radius (r) [44].

$$g(r) = \frac{P(r)}{\rho} \tag{1}$$

$$P(r) = 4\pi r^2 \rho g(r) \tag{2}$$

3. Results and discussion

3.1. Unit cell and bulk structure

The hexagonal unit cell consisting of a periodic cell containing 16 carbon atoms and the bulk structure are shown in Fig. 2(a) and (b), respectively. Fig. 2(b) shows that the bulk structure constructed from the unit cell, by doubling the a,b and c lattices, was successfully optimised. The following lattice parameters, namely a, b = 2.462 Å and c = 11.101 Å, and angles of α, β = 90°, and γ = 120° were obtained for both the unit cell and the bulk structure. This correlates well with published crystallographic data by Nixon et al. [30], namely a, b = 2.46 Å and c = 11.06 Å, and angles of α, β = 90°, and γ = 120° A table (Table S1) containing the lattice coordinates of the unit cell is provided in the Supplementary Information.

The relaxed C—C distances, within a layer, were determined to be 1.417 Å, and an interlayer spacing of 3.445 Å was obtained. These values correlate well with values of 1.42 Å and 3.4 Å as reported by Jurkiewicz et al. [11], and 1.42 Å and 3.35 Å reported by Cowlard et al. [3]. The energy for the optimised unit cell was calculated as −58.154 eV/atom.

3.2. Pristine slabs

The k-point optimisation, illustrated in the supplementary

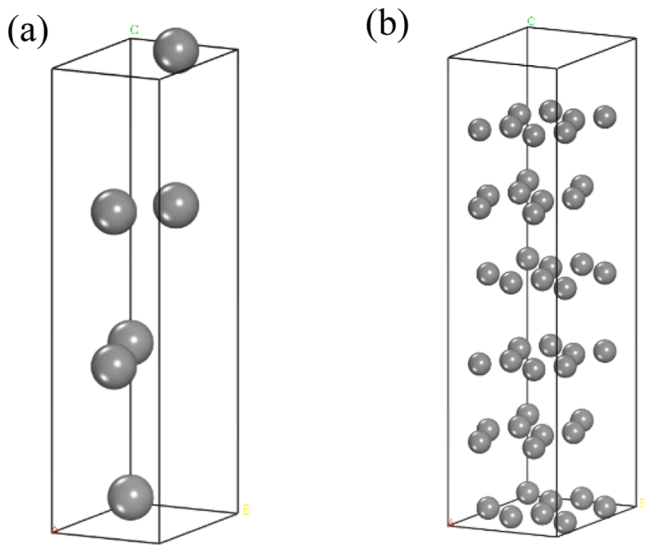

Fig. 2. Images of the (a) R3 primitive unit cell and (b) R3 bulk structure.

information (Figure S1), demonstrated that the energy converged at a 5 × 5 × 1 k-point grid, achieving the smallest variation in energies with a difference <10 meV. Consequently, this configuration will be adopted for subsequent geometric optimisation.

The number of carbon layers in the slab was investigated (supplementary information Figure S2). It was found that the energy per atom difference between 5 layers and 15 layers is 2.1 × 10^{-4} eV/atom. This indicates that 5 layers are sufficient to keep calculations accurate but keep the overall number of atoms low to save on computational time.

After the identification of the optimal parameters, namely, the k-point and slab thickness, the slab model could be developed. Two slab models were constructed, one with 582 carbon atoms and another with 1080 carbon atoms. Both slabs had five carbon layers and a 20 Å vacuum gap. The smaller slab model, shown in Fig. 3(a), is described with lattice parameters a, b, and c of 14.76 Å, 17.74 Å and 42.35 Å, respectively. The larger slab containing 1080 atoms, shown in Fig. 3(b), is described with lattice parameters a, b, and c of 22.16 Å, 26.63 Å and 42.27 Å, respectively.

3.3. Defect-induced slabs

As mentioned in the method section a systematic approach was employed for the removal of 10 % of carbon atoms from the pristine slab. Following the removal process, the configuration of the atomic lattice was perturbed, causing a disruption in the original structural atomic arrangement. Subsequently, to the alteration of the atomic structure, the system was subjected to a relaxation process. This was executed by employing a geometric optimisation, allowing the structure to reach a new equilibrium state. The structure at equilibrium will be referred to as the DI-GC slab. Several defect-induced GC slabs were created. Creating the DI-GC slabs were done to find a structure that best represents the GC model proposed by Harris et al. [2] and Jurkiewicz et al. [11]. Five of the DI-GC slabs that best represent the GC model are displayed in Fig. 4.

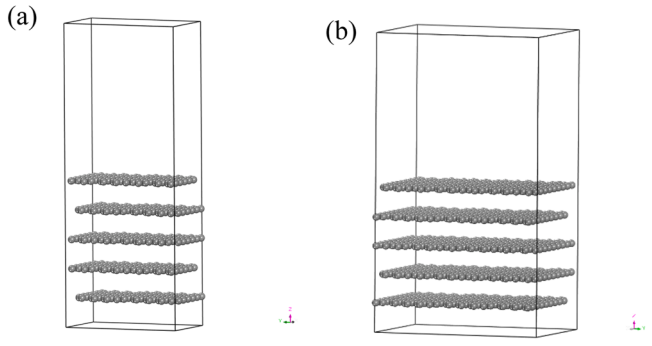

Fig. 3. (a) R3 slab containing 582 carbon atoms, and (b) larger slab containing 1080 carbon atoms with a 20 Å vacuum gap.

As seen in Fig. 4, large differences in the model's structure are observed after the relaxation post-defect induction. These large differences indicate that the DI-GC model is sensitive to minor changes and thus multiple DI-GC slabs had to be created and theoretical XRD data generated (the XRD's can be seen in Supplementary Information, namely Figure S3). Fig. 5, shows an example of the theoretical XRD, that was generated by taking the average of the peaks and intensities from the nine cuts of the DI-GC model shown in Fig. 4(e). Eight peaks with an intensity higher than 10 arb. units, were identified for the DI-GC model, namely at 8.75°, 13.2°, 13.7°, 14.4°, 16.3°, 17.6°, 35.5° and 40.2°.

3.4. Jurkiewicz models

The reduction in model size, as described in the methods section, induced limitations on the theoretical XRD results, such as removing the long-range periodicity and inducing short-range periodicity. The short-range periodicity will force short-range order in the XRD profiles.

Experimental XRD spectra of GC would normally show as broad diffuse peaks, however due to the short-range periodicity the theoretical XRD will show a reduced number of sharp specific ordered peaks. A substantial amount of XRD data was generated for each model, namely 9 cuts for each of the four formation temperatures. Fig. 6 presents the diffractogram for the JGC_2000 model, showcasing the XRD data for the 9 cuts. The XRD spectra for the other temperatures are detailed in the Supplementary Information, specifically in Figure S4.

The detailed analysis for the JGC_2000 model, presented in Fig. 7, showed that if the spectra of the various cuts are compared, unique XRD peaks are easily identified. This variability highlights the complexity of GC structure, necessitating a methodical approach to generate an average XRD profile that accurately represents the entirety of the structure. To achieve this, a process of averaging the XRD peaks obtained from various cuts was employed. Fig. 8 shows the consolidated average XRD peak data for the 9 cuts of the JGC_2000 model.

Seven peaks with an intensity higher than 10 arb. units, were obtained for the JGC_2000 model, as shown in Fig. 8, namely at 8.75°, 13.2°,17.6°, 35.5°, 38.3°, 40.2° and 42.6°. The consolidated average XRD peaks for the other temperatures are detailed in the Supplementary Information, specifically in Figure S5.

3.5. Comparison of models

By comparing the XRD spectra of the DI-GC and JGC models (Figs. 5 and 7), it becomes evident that there is a significant correlation between the two. Both XRD patterns exhibit matching peaks at 8.75°, 13.2°, 17.6°, 35.5°, and 40.2°, with similar intensities. These consistent peaks suggest that the structures of the DI-GC and JGC models are closely related. The alignment of these diffraction peaks indicates that the two models possess similar lattice parameters and phase compositions. This similarity in the XRD patterns implies that the DI-GC and JGC models share comparable structural characteristics, reinforcing the notion that their underlying structures are fundamentally alike.

GC can be synthesised at various temperatures, and it has been demonstrated that the temperature used during GC formation significantly affects the structure of the GC. GC's formed at higher temperature exhibit less "crumpling" and arranged in a more ordered form [11]. As the formation temperature increases kinetic energy allows the carbon atoms to overcome energy barriers, hence the atoms arrange in a more ordered form, with layer distortion, lowering the number of visible peaks in XRD spectra. Hence, XRD data of the DI-GC model was

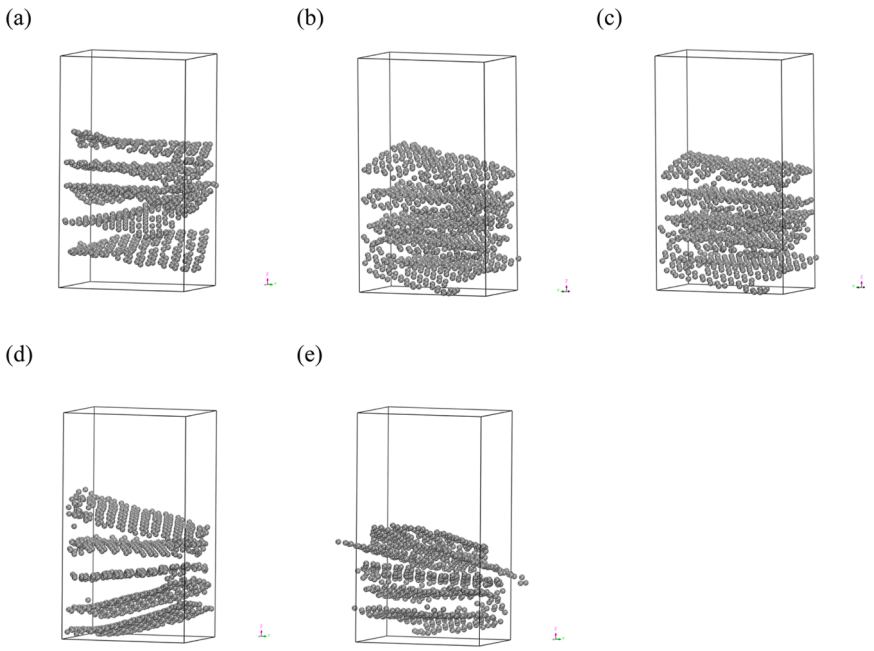

Fig. 4. Five examples of defect-induced GC (DI-GC) slabs.

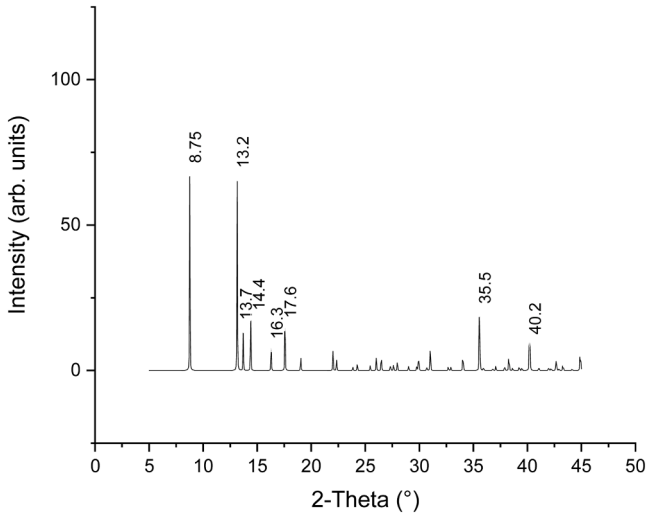

Fig. 5. The average XRD of the DI-GC model (Figure 4(e)) using the combined data for the nine cuts.

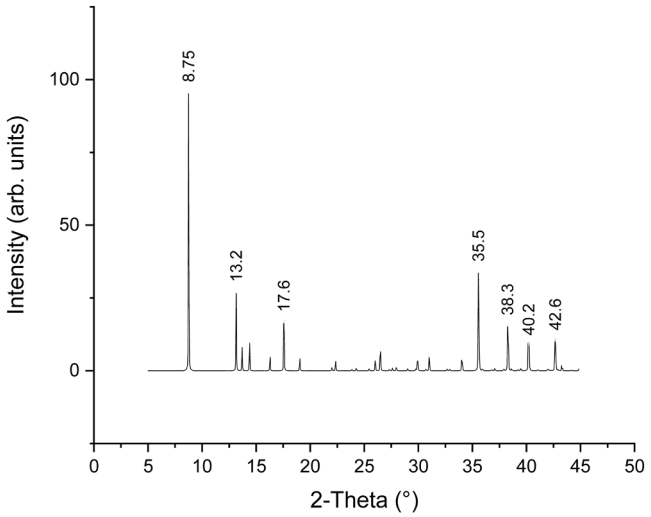

Fig. 7. The average XRD of the JGC_2000 model using the combined data for the nine cuts of JGC_2000.

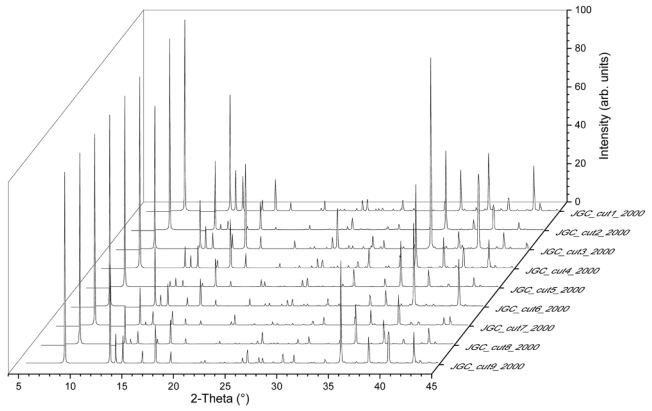

Fig. 6. The modelled XRD spectra of the 9 cuts of the 2000 °C JGC model.

compared to XRD models of different formation temperatures, as seen in Fig. 8, to determine the GC model's approximate formation temperature. The position and intensity of the peaks in the XRD spectra presented in Fig. 8 are detailed in Table 1.

The data from Table 1 indicates the peak positions and intensity, only peaks that were above an intensity of 5 and a maximum of 10 peaks were listed. Furthermore, the XRD analysis of both the JGC_2000 model and the newly developed DI-GC model shows the strongest correlation, with matching peaks at 8.75°, 13.2°, 17.6°, 35.5°, and 40.2°. Such a correlation suggests that the DI-GC model's performance is comparable to the findings published by Jurkiewicz et al. [11]. Additionally, the highest degree of correlation is observed between the DI-GC model and the JGC models are between 1500 °C and 2000 °C, suggesting that the structural characteristics of this DI-GC model are representative between these formation temperatures.

Fig. 9 shows the combined average XRD peak data for all the JCG models across the formation temperatures ranging from 800° to 2500 °C

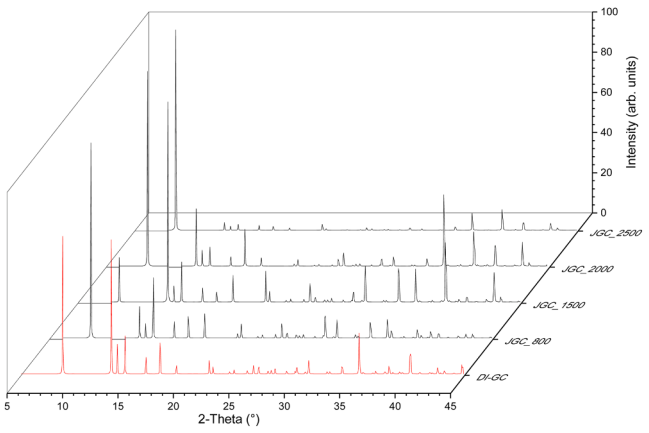

Fig. 8. Average XRD peaks for JCG models and the DI-GC model (shown in red), highlighting the precision in crystalline structure representation across temperatures from 800° to 2500 °C.

and the DI-GC model. When comparing the DI-GC model with the JGC models, the XRD peaks match closely which stands as a verification of the current study's methodology in simulating and understanding the complex structure of GC materials.

In addition to the simulated XRD patterns, the RDF were calculated for the DI-GC and JGC models, as shown in Fig. 10. To compare RDF values across the different models, the normalized g(r) fraction was used. This fraction was determined using Eq. (3), where the RDF value g (r) is divided by the maximum value, $g(r)_{max}$.

$$g(r)Fraction = \frac{g(r)}{g(r)_{max}} \quad (3)$$

The JGC models reveal that as the formation temperature increases, the RDF peaks become more distinct, indicating an improvement in crystalline order. The RDF profile of the DI-GC model aligns closely with those of the JGC models, validating that the DI-GC model accurately represents the structures developed by Jurkiewicz et al. [11]. Furthermore, the RDF analysis suggests that the DI-GC model corresponds to a formation temperature range of 800 °C to 1500 °C. This finding complements the XRD simulations, which indicated a close match between the DI-GC model and the 1500 °C–2000 °C temperature range. Together, these results imply that the DI-GC model is most consistent with a formation temperature of 1500 °C. The apparent discrepancy between the temperature ranges obtained from XRD and RDF can be attributed to the different structural features each technique examines. While RDF is more sensitive to short- and medium-range atomic order, XRD captures long-range crystallinity. This suggests that the DI-GC model represents a transitional structure, incorporating features of both lower-temperature and higher-temperature regimes.

4. Conclusion

This study successfully optimised the parameters of both the bulk and unit cells models, achieving lattice parameters and angles that align closely with established literature values [30]. The energy of the optimised unit cell was determined to be −58.154 eV/atom, indicating a

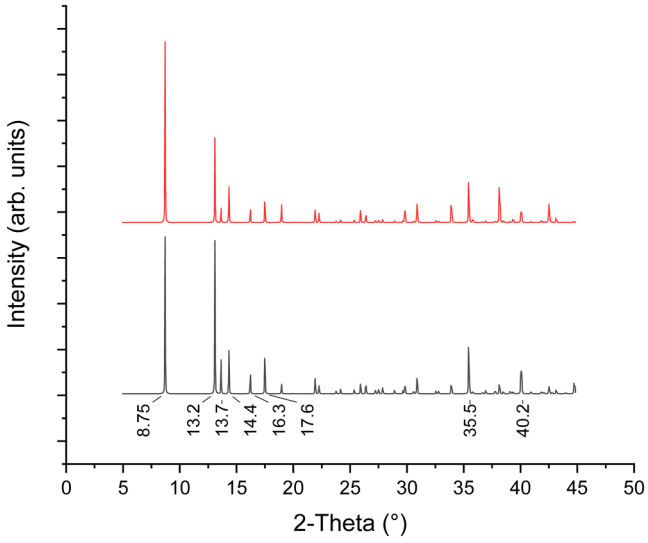

Fig. 9. Average GC (black) compared to the cumulative JGC (red) over the formation range 800 °C - 2500 °C.

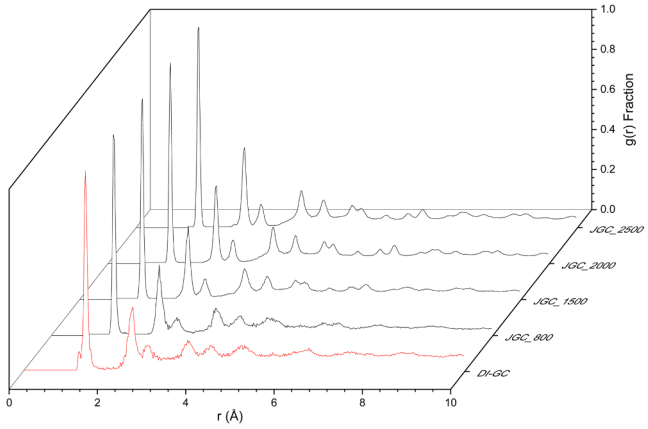

Fig. 10. Radial distribution function of DI-GC (red) and JGC models (black) across the formation temperatures of 800 °C - 2500 °C.

Table 1
List of XRD peaks for the average XRD spectra.

GC		JGC_800		JGC_1500		JGC_2000		JGC_2500	
2-Theta (°)	Intensity (arb units)	2-Theta (°)	Intensity (arb units)	2-Theta (°)	Intensity (arb units)	2-Theta (°)	Intensity (arb units)	2-Theta (°)	Intensity (arb units)
8.75	68.7	8.75	97.4	8.75	22.2	8.75	97.2	8.75	100.0
13.2	67.1	13.2	15.7	13.2	100.0	13.2	28.6	38.3	10.3
13.7	14.8	14.4	30.1	14.4	20.0	17.6	18.3		
14.4	19.0	17.6	10.7	19.1	13.3	35.5	35.6		
16.3	8.22	19.1	12.1	22.0	15.4	38.3	17.1		
17.6	15.5	29.9	10.9	31.0	17.8	40.2	10.3		
35.5	20.3			34.0	16.8	42.6	12.0		
40.2	9.89			35.5	16.5				
				38.3	29.7				
				42.6	14.6				

stable configuration. The relaxed C—C distances and interlayer spacing obtained further corroborate the accuracy of the optimisation process, aligning well with previously reported values [3], thus validating the computational approach used. The 5 × 5 × 1 k-point grid was used for all geometric optimisations, balancing computational efficiency with accuracy. This optimisation was crucial for the development of a slab model that accurately reflects the structural characteristics of carbon layers, concluding in a 1080 carbon atom model that provides a more realistic representation of pristine and defect-induced slabs.

The systematic introduction of defects and subsequent iterative geometric optimisation enabled the formation of the DI-GC model. This approach helped the identification of slab configurations that closely resemble the GC models proposed by Jurkiewicz et al. [11]. The model closely matched the published models, that were developed based on experimental structure data of GC. However, this model was derived from inducing defects into a pristine surface and allowing the system to reorder into the characteristic GC form. The XRD analysis, obtained specifically through the division of the GC models into nine distinct sections, allowed for a detailed examination of the XRD spectra at various formation temperatures. This methodological refinement enabled the reduction of data complexity, allowing for a more distinct comparison between models. The average XRD spectra presented consolidate the findings, offering a comprehensive overview of the structural evolution of the GC material. The inclusion of RDF analysis further reinforced the validation of the DI-GC model by providing additional structural correlation, when compared to the JGC models, highlighting their comparable accuracy. The strong agreement between the published models [10,11] and those developed in this study, especially the close correlation of peak positions and intensities, demonstrates the strength of the computational methods employed.

CRediT authorship contribution statement

K. Meerholz: Writing – original draft, Visualization, Validation, Methodology, Investigation, Data curation, Conceptualization. **A. Falch:** Writing – review & editing, Supervision. **C.G.C.E. van Sittert:** Writing – review & editing, Supervision, Conceptualization.

Declaration of competing interest

The authors declare the following financial interests/personal relationships which may be considered as potential competing interests:

K Meerholz reports financial support was provided by National Research Foundation (NRF), South Africa. If there are other authors, they declare that they have no known competing financial interests or personal relationships that could have appeared to influence the work reported in this paper.

Acknowledgements

The author acknowledges financial assistance provided by the National Research Foundation (NRF) in respect to the costs of this study (grant number 102104). Additionally, the Centre for High Performance Computing (CHPC) for the support and resources, including the use of hardware and software, which without this study would not be possible. Lastly, acknowledgment to the North-West University South Africa for the financial and resource support.

Supplementary materials

Supplementary material associated with this article can be found, in the online version, at doi:10.1016/j.cartre.2025.100466.

Data availability

Data will be made available on request.

References

[1] L.A. Pesin, Review: structure and properties of glass-like carbon, J. Mater. Sci. 37 (1) (2002) 1–28, https://doi.org/10.1023/A:1013100920130Scopus. Review.
[2] P.J.F. Harris, Fullerene-related structure of commercial glassy carbons, Philos. Mag. 84 (29) (2004) 3159–3167, https://doi.org/10.1080/14786430410001720363.
[3] F.C. Cowlard, J.C. Lewis, Vitreous carbon — A new form of carbon, J. Mater. Sci. 2 (6) (1967) 507–512, https://doi.org/10.1007/BF00752216.
[4] A. Dekanski, J. Stevanović, R. Stevanović, B.Ž. Nikolić, V.M. Jovanović, Glassy carbon electrodes, characterization and electrochemical activation, Carbon N Y 39 (8) (2001) 1195–1205, https://doi.org/10.1016/S0008-6223(00)00228-1.
[5] S. Yamada, H. Sato, Some physical properties of glassy carbon, Nature 193 (4812) (1962) 261–262, https://doi.org/10.1038/193261b0.
[6] P.J.F. Harris, Structure of non-graphitising carbons, Int. Mater. Rev. 42 (5) (1997) 206–218, https://doi.org/10.1179/imr.1997.42.5.206.
[7] D. Crawford, D. Johnson, High-resolution electron microscopy of high-modulus carbon fibres, J. Microsc. 94 (1) (1971) 51–62.
[8] G.M. Jenkins, K. Kawamura, Structure of glassy carbon, Nature 231 (5299) (1971) 175–176, https://doi.org/10.1038/231175a0. ArticleScopus.
[9] L. Hawelek, P. Wlodarczyk, A. Hudecki, M. Lis, P. Zackiewicz, K. Jurkiewicz, J. Szade, J. Kubacki, K. Balin, H.E. Fischer, et al., The atomic scale structure of glass-like carbon obtained from fullerene extract via spark plasma sintering, Carbon N Y 110 (2016) 172–179, https://doi.org/10.1016/j.carbon.2016.09.017.
[10] K. Jurkiewicz, S. Duber, A. Burian, Paracrystalline structure of glass-like carbons, Int. J. Appl. Glass Sci. 7 (3) (2016) 355–363, https://doi.org/10.1111/ijag.12186. ArticleScopus.
[11] K. Jurkiewicz, S. Duber, H.E. Fischer, A. Burian, Modelling of glass-like carbon structure and its experimental verification by neutron and X-ray diffraction, J. Appl. Crystallogr. 50 (1) (2017) 36–48, https://doi.org/10.1107/S1600576716017660.
[12] M.I. Nathan, J.E. Smith, K.N. Tu, Raman spectra of glassy carbon, J. Appl. Phys. 45 (5) (1974), https://doi.org/10.1063/1.1663599, 2370-2370.
[13] S.F. Parker, S. Imberti, S.K. Callear, P.W. Albers, Structural and spectroscopic studies of a commercial glassy carbon, Chem. Phys. 427 (2013) 44–48, https://doi.org/10.1016/j.chemphys.2013.05.002.
[14] R. Perret, W. Ruland, X-ray small-angle scattering of glassy carbon, J. Appl. Crystallogr. 5 (3) (1972) 183–187, https://doi.org/10.1107/s0021889872009161.
[15] V. Petkov, R.G. Difrancesco, S.J.L. Billinge, M. Acharya, H.C. Foley, Local structure of nanoporous carbons, Philos. Mag. Part B 79 (10) (1999) 1519–1530, https://doi.org/10.1080/13642819908218319.
[16] A.J. Stone, D.J. Wales, Theoretical studies of icosahedral C60 and some related species, Chem. Phys. Lett. 128 (5–6) (1986) 501–503, https://doi.org/10.1016/0009-2614(86)80661-3.
[17] L. Hawełek, J. Kołoczek, A. Bródka, J.C. Dore, V. Honkimäki, A. Burian, Structural studies of disordered carbons by high-energy X-ray diffraction, Philos. Mag. 87 (32) (2007) 4973–4986, https://doi.org/10.1080/14786430701594038.
[18] K. Jurkiewicz, S. Duber, H.E. Fischer, A. Burian, Modelling of glass-like carbon structure and its experimental verification by neutron and X-ray diffraction, J. Appl. Crystallogr. 50 (1) (2017), https://doi.org/10.1107/s1600576716017660.
[19] Y. Gogotsi, Graphite polyhedral crystals, Science 290 (5490) (2000) 317–320, https://doi.org/10.1126/science.290.5490.317.
[20] P.J.F. Harris, Z. Liu, K. Suenaga, Imaging the atomic structure of activated carbon, J. Phys.: Condens. Matter 20 (36) (2008) 362201, https://doi.org/10.1088/0953-8984/20/36/362201.
[21] A. Szczygielska, A. Burian, J.C. Dore, Paracrystalline structure of activated carbons, J. Phys.: Condens. Matter 13 (24) (2001) 5545–5561, https://doi.org/10.1088/0953-8984/13/24/301.
[22] J.C. Palmer, J.K. Brennan, M.M. Hurley, A. Balboa, K.E. Gubbins, Detailed structural models for activated carbons from molecular simulation, Carbon N Y 47 (12) (2009) 2904–2913, https://doi.org/10.1016/j.carbon.2009.06.037.
[23] L. Hawelek, A. Brodka, J.C. Dore, V. Honkimäki, A. Burian, Fullerene-like structure of activated carbons, Diam. Relat. Mater. 17 (7–10) (2008) 1633–1638, https://doi.org/10.1016/j.diamond.2008.01.035.
[24] L. Hawelek, N. Woznica, A. Brodka, V. Fierro, A. Celzard, A. Bulou, A. Burian, Graphene-like structure of activated anthracites, J. Phys. Condens. Matter 24 (49) (2012) 495303, https://doi.org/10.1088/0953-8984/24/49/495303.
[25] X. Jiang, C. Århammar, P. Liu, J. Zhao, R. Ahuja, The R3-carbon allotrope: a pathway towards glassy carbon under high pressure, Sci. Rep. 3 (2013) 1877, https://doi.org/10.1038/srep01877. PMC.
[26] BIOVIA. CASTEP, Materials Studio. Dassault Systèmes Customer Support: 2019.
[27] S.J. Clark, M.D. Segall, C.J. Pickard, P.J. Hasnip, M.J. Probert, K. Refson, M. C. Payne, First principles methods using CASTEP, Zeitsch. Kristallogr. 220 (5–6) (2005) 567–570, https://doi.org/10.1524/zkri.220.5.567.65075. Article.
[28] *National intergrated cyber infrastructure system, centre for high performance computing* 2017. https://www.chpc.ac.za/index.php/resources/lengau-cluster (accessed 2022, 29 September).
[29] P. Trucano, R. Chen, Structure of graphite by neutron diffraction, Nature 258 (5531) (1975) 136–137, https://doi.org/10.1038/258136a0.
[30] D. Nixon, G. Parry, A.R.J.P. Ubbelohde, Order-disorder transformations in graphite nitrates, Proc. R. Soc. Lond. Ser. A Mathe. Phys. Sci. 291 (1426) (1966) 324–339.
[31] A. Jain, S.P. Ong, G. Hautier, W. Chen, W.D. Richards, S. Dacek, S. Cholia, D. Gunter, D. Skinner, G. Ceder, et al., Commentary: the materials project: a materials genome approach to accelerating materials innovation, APL Mater. 1 (1) (2013) 011002, https://doi.org/10.1063/1.4812323.

[32] J.P. Perdew, K. Burke, M. Ernzerhof, Generalized gradient approximation made simple, Phys. Rev. Lett. 77 (18) (1996) 3865–3868, https://doi.org/10.1103/PhysRevLett.77.3865.
[33] H.J. Monkhorst, J.D. Pack, Special points for Brillouin-zone integrations, Phys. Rev. B 13 (12) (1976) 5188–5192, https://doi.org/10.1103/PhysRevB.13.5188.
[34] D.D. Koelling, B.N. Harmon, A technique for relativistic spin-polarised calculations, J. Phys. C: Solid State Phys. 10 (16) (1977) 3107–3114, https://doi.org/10.1088/0022-3719/10/16/019.
[35] D.E. Nixon, G.S. Parry, A.R.J.P. Ubbelohde, Order-disorder transformations in graphite nitrates, Proc. R. Soc. Lond. Ser. A Mathe. Phys. Sci. 291 (1426) (1966) 324–339, https://doi.org/10.1098/rspa.1966.0098.
[36] BIOVIA, MS Modelling Datasheet: Reflex Tools, 2005. San Diego.
[37] *BIOVIA materials Sudio Reflex Tools QPA Datasheet*; BIOVIA, 2021.
[38] G. Vignaud, A. Gibaud, REFLEX: a program for the analysis of specular X-ray and neutron reflectivity data, J. Appl. Crystallogr. 52 (2019) 201–213, https://doi.org/10.1107/S1600576718018186.
[39] Y.M. Mos, A.C. Vermeulen, C.J. Buisman, J. Weijma, X-ray diffraction of iron containing samples: the importance of a suitable configuration, Geomicrobiol. J. 35 (6) (2018) 511–517.
[40] W. Pitschke, H. Hermann, N. Mattern, The influence of surface roughness on diffracted X-ray intensities in Bragg–Brentano geometry and its effect on the structure determination by means of Rietveld analysis, Powder Diffr. 8 (2) (1993) 74–83, https://doi.org/10.1017/S0885715600017875. From Cambridge University Press Cambridge Core.
[41] W.H. Bragg, W.L. Bragg, The reflection of X-rays by crystals, Proc. R. Soc. Lond. Ser. A Contain. Pap. Mathe. Phys. Charac. 88 (605) (1913) 428–438, https://doi.org/10.1098/rspa.1913.0040.
[42] M. Birkholz, Thin Film Analysis By X-ray Scattering, John Wiley & Sons, 2006.
[43] F. Li, J.S. Lannin, Radial distribution function of amorphous carbon, Phys. Rev. Lett. 65 (15) (1990) 1905–1908, https://doi.org/10.1103/PhysRevLett.65.1905.
[44] K. Younge, C. Christenson, A. Bohara, J. Crnkovic, P. Saulnier, A model system for examining the radial distribution function, Am. J. Phys. 72 (9) (2004) 1247–1250, https://doi.org/10.1119/1.1758228 (acccessed 12/5/2024).